An integrated numerical model for investigating guided waves in impact-damaged composite laminates

B. Zhang[a,*], X.C. Sun[a], M.J. Eaton[b], R. Marks[b],

A. Clarke[b], C.A. Featherston[b], L.F. Kawashita[a], S.R. Hallett[a]

[a]Advanced Composites Centre for Innovation and Science (ACCIS),

University of Bristol, Queen's Building, University Walk, Bristol BS8 1TR, UK

[b] Cardiff School of Engineering,

Cardiff University, Queen's Buildings, The Parade, Cardiff CF24 3AA, Wales, UK

Abstract

This paper presents a novel numerical technique that combines predictions of impact-induced damage and subsequent ultrasonic guided-wave propagation in composite laminates, with emphasis on the development and verification of the modelling framework. Delamination and matrix cracking are considered in the modelling technique, which is validated by experimental measurements on a carbon-fibre/epoxy plate using a drop-weight impact tower and a scanning laser vibrometer. Good agreement has been found between simulations and experiments regarding the impact response and global-local wavefields. Effects of these two damage modes, damage extent and multiple impacts on guided waves are studied using the modelling tool. Matrix cracking leads to lower wavefield scattering compared with delamination, particularly in un-damaged regions. The modelling strategy can provide valuable guidelines for optimising health-monitoring arrangements on composite structures that are susceptible to impacts, and the guided-wave model can also be integrated with other numerical models for predicting internal flaws in composite laminates.

Keywords: Impact behaviour; Guided waves; Laminates; Finite element analysis (FEA)

*Corresponding author: b.zhang@bristol.ac.uk (B. Zhang); +44(0) 117 33 15311

1. Introduction

Owing to high specific stiffness and strength, fibre-reinforced plastic (FRP) composite laminates are increasingly being used in many industries, including aerospace, automotive, civil, electronics and marine. Excellent in-plane properties can be achieved by tailoring the fibre/matrix materials and stacking sequence of laminates. One of the major concerns when designing laminated structures is their relative weaker through-thickness properties. As a result, composite laminates are susceptible to interlaminar fracture (delamination) when exposed to an impact threat, e.g. dropped tools and hail. Typical damage modes due to low-velocity impact also include intralaminar failure, such as matrix cracking, fibre breakage and fibre/matrix debonding [1]. Low-velocity impact damage significantly degrades the residual strength and fatigue life of a laminated structure [2,3], with the degradation severity increasing with impact energy [4]. Therefore, a number of non-destructive testing (NDT) technologies have been developed to evaluate the structural integrity of composite laminates, including acoustic emission [5], eddy current effect [6], electrical resistance measurement [7], ultrasonic C-scan and tomographic imaging [8].

Ultrasonic guided waves have been widely used to evaluate the integrity of engineering structures, due to their ability to propagate over considerable distances and excellent sensitivity to the presence of defects in the propagation path. Given that composite laminates are generally thin plate-like structures, the resulting Lamb waves feature two simultaneously existing modes, namely the symmetric (S) and anti-symmetric (A) modes [9]. Guided waves are usually generated by an excitation source, typically a piezoelectric transducer coupled with the laminate. Once these waves have been generated, the structural integrity of the laminate can be evaluated by the transducer itself or other sensors coupled to the laminate. This procedure can take place during a

maintenance inspection or while the structure is in service. Guided-wave propagation in composite laminates is a very complex phenomenon due to a number of factors, including (i) the anisotropic properties of individual laminae (plies), (ii) the fact that laminates are usually made of plies with different fibre orientations, and (iii) the dispersive nature of guided waves. Impact-induced damage further enhances the complexity, by scattering and reflecting guided waves. As a result, it becomes practically difficult to derive analytical solutions for the detailed guided-wave propagation behaviour of impact-damaged laminates. Hence, most of the research on guided-wave propagation in impacted laminates has been based on experiments and numerical modelling. Regarding experimental characterisation, low-velocity impact damage is normally introduced into a laminate through drop weight [10–12] or quasi-static indentation tests [13–15]. The location and size of damage and/or flaws can be ascertained by the phase shift and amplitude difference between the sensing signals acquired before and after impact [10,11,16]. Both of the sensing indicators increase with the damage size. The detection accuracy can be improved by increasing the number of signal acquisition points, as illustrated in [12] by a 2-dimensional scanning method. Another experimental approach for evaluating the health condition of an impact-damaged laminate is to examine the guided wavefield acquired by a scanning laser vibrometer (SLV). It provides more intuitive observations of guided-wave propagation, as well as its interaction with damage. The combination of time-domain and frequency-domain analyses of the guided wavefield aids more accurate prediction of the impact-induced damage [14,17].

Experimental characterisation of structural health monitoring (SHM) systems is costly and time-consuming, attributed to various configuration parameters, including the laminate material, the stacking sequence and the impact energy. It is also difficult to visualise wave propagation inside the laminates during experiments. Hence, several finite

element (FE) models were proposed in [15,18–24] to investigate the influence of the dominant impact damage mechanism, i.e. delamination on guided waves. Delamination was assumed to have an idealised geometry and wave scattering due to delamination was examined in these models. On the other hand, Leckey et al. developed a 3D elasto-dynamic finite integration model that incorporated realistic impact-induced delamination geometries measured by X-ray computed tomography (CT) scanning [15], indicating that the realistic geometry of impact-induced delamination should be taken into account in order to improve the prediction quality of numerical models. In addition, the overall impact damage was represented by simply degrading material properties in the FE models proposed in [24,25].

Whilst numerical modelling techniques for predicting low-velocity impact damage are quite well advanced [26–28], modelling techniques that combine these simulations with the analysis of ultrasonic guided-wave propagation have not been so far put forward in the literature. Such an integrated modelling capability is imperative in the development of NDT and SHM systems for composites, since it completes the virtual characterisation process from impact to guided-wave propagation using numerical simulation, thus saving considerable time in comparison with experimental studies. Therefore, the objective of the present work is to develop an integrated numerical modelling methodology for characterising guided waves in composite laminates after undergoing low-velocity impact. The numerical strategy consists of a model that predicts impact-induced damage including delamination and matrix cracks, a guided-wave model that imports the predicted damage data and analyses guided-wave propagation in the damaged laminate, and a damage transfer code. Delamination and material cracking are both directly meshed in the guided-wave model. Section 2 first provides experimental characterisation of a quasi-isotropic carbon FRP plate. Section 3 presents detailed descriptions of the novel

impact-ultrasonic modelling tool. Comparisons between experimental measurements and numerical results are then detailed in Section 4 to verify and validate the methodology. The modelling framework is employed in Section 5 to investigate the effects of these two damage modes, damage extent and multiple impacts on guided-waves.

2. Experimental characterisation

2.1. Specimen preparation

A composite plate with the dimensions of 4 × 200 × 300 mm^3 (thickness × width × length) was manufactured from 32 plies of Hexcel® IM7/8552 pre-preg material, stacked following the sequence of $[45_2/0_2/90_2/\text{-}45_2]_{2S}$. The quasi-isotropic laminate was vacuum bagged and cured in an autoclave following the material manufacturer's recommended cycle (2 h at 180 °C with 180 psi pressure). Note that the in-plane dimensions of the plate are double that of the more commonly used ASTM D7136 standard [29] in order to give a panel size that is more realistic for guided-wave propagation. Fig. 1 shows the analytical dispersion curves created for the laminate using the software package DISPERSE® and the material properties given in Table 1.

2.2. Low-velocity impact

The plate was impacted at its centre using an Instron® Dynatup 9250 HV drop-weight impact tower, whose impactor had a 16 mm diameter hemispherical shape and a 6.3 kg weight. In order to accommodate the larger than standard plate, a new support fixture was designed and manufactured. Based on the scaling between the ASTM standard plate [29] and the plate tested in this study, the support frame dimensions were doubled to 250 × 150 mm^2, as compared in Fig. 2. The same four rubber-tipped clamps were used. The support fixture was made of steel, and the flatness tolerance of the top surface was kept within 0.1 mm to ensure that each opening edge provided uniform support to the plate during impact. The impact energy for this case was 12 J, so that damage introduced

by the low-velocity impact test was dominated by delamination and matrix cracks. The projected delamination area in the plate was inspected by ultrasonic C-scan.

2.3. Scanning laser vibrometry

The laser vibrometry study was undertaken using a 3D scanning laser vibrometer (Polytec® PSV-500-3D-M). The test set-up is presented in Fig. 3. Through the use of three laser heads the system can resolve wave velocities in three principal directions, i.e. two in-plane and one out-of-plane. Ultrasonic excitation was achieved using a Mistras Group Ltd. *Nano30* piezoelectric transducer (8 mm diameter), placed at the middle of the left-hand short side of the plate on the impactor side. The transducer was fixed with silicon RTV adhesive (Loctite® 595) which also provided suitable acoustic coupling. The transducer was excited by a 140 kHz five-cycle sine wave modulated by a Hanning window (300 V pp) generated by a Mistras Group Ltd. Arbitrary Waveform Generator (*WaveGen 1410*). The excitation frequency was chosen to provide a balance between sensitivity to damage and computational cost of models as presented in the next section. The signal was Hanning window modulated to limit the signal bandwidth so that only zero-order modes were excited (Fig. 1). Apart from the first asymmetric (A_0) and symmetric (S_0) modes, the zero-order shear horizontal mode SH_0 was also generated under the current frequency. However, the asymmetric mode has a shorter wavelength than other two modes under the excitation frequency, thus it is more sensitive to damage. Furthermore, considering that the plate was excited in the thickness direction, which was dominated by the A_0 mode, the emphasis of this study is placed on the A_0 mode. The panel was held in low density foam supports (Fig. 3), to provide some acoustic isolation, and mounted to an aluminium frame. The supports were arranged such that the panel could be removed and replaced into the same position, following impact testing. A thin coating of retroreflective glass spheres was applied to the panel, using a light spray

adhesive, to enhance the backscattered laser signal. Vibrometry measurements of the propagating waves were made at 2 mm intervals (total of 14,928 data points). Data were acquired at a velocity sensitivity of 200 mm/s, with a 2.56 MHz sample rate and 100 averages were made for each measurement to improve the signal to noise ratio. The data acquired was sufficient to verify the proposed modelling strategy. One objective of the work was to consider how the guided waves propagated to the sensors at locations remote from the impact location.

3. Impact-ultrasonic modelling tool

As shown in Fig. 4a, the modelling framework comprises an impact model, a guided-wave model and a damage transfer MATLAB® code. The impact model was employed to predict low-velocity impact damage in the laminate. The MATLAB® code then imported the predicted damage information into the guided-wave model, which then simulated ultrasonic wave propagation in the laminate. Both models were created according to the experimental set-up described in the last section. For ease of expression, the *global* coordinate system *X*-*Y*-*Z* is established with its origin coincident with the lower left corner of the bottom surface of the laminate, as shown in Fig. 4a. The global *X*-axis and *Y*-axis follow the length and width of the laminate, respectively. The *local* coordinate system *x*-*y*-*z* of a ply has its origin coincident with the centre of the ply and its *x*-axis following the fibre direction of the ply.

3.1. Impact model

The impact model shown in Fig. 4a used a novel global-local approach developed by the authors in [30,31] to describe the laminate. The impact sensitive region with a 50 mm radius was modelled by 3D continuum (i.e. ‘solid’) elements, while shell elements were used for the surrounding region where damage was not expected to occur. The solid-element part was created using a high-fidelity modelling approach proposed in [28].

Specifically, each 'ply block' (i.e. two neighbouring plies with the same orientation) in the solid-element part was represented by a ply-level mesh as shown in Fig. 4b. The ply-level mesh was oriented along the fibre direction for each ply block. Thus, the solid-element part comprised 16 layers of ply-level meshes. In order to predict potential matrix cracks, the ply-level mesh also possessed three pairs of cohesive element strips symmetrically inserted on two sides of the local *x*-axis, with separations of 3 mm, 7 mm and 13 mm, respectively [28]. All the cohesive elements for modelling matrix cracking were zero thick and 0.2 mm long. Each interlaminar interface was modelled using a layer of 0.01 mm thick cohesive mesh, one quarter of which is shown in Fig. 4c. Each element of the cohesive mesh has 0.2×0.2 mm^2 in-plane dimensions in the region of interest (ROI) where delamination is expected to occur. Considering that a ply may have different element dimensions from its adjacent interfaces, the degrees of freedom (DOFs) between them were linked by a 'tied contact', which was defined by the well-known penalty algorithm [32]. Cohesive elements for modelling delamination and matrix cracks both followed the same failure criteria [33,34], which is briefly described below. Stress and displacement prior to failure are related by an elastic stiffness, which is indicated by K_I for mode I (opening) and K_{II} for mode II (shearing). Interlaminar failure initiation and evolution are controlled by a quadratic stress criterion and a power law criterion, respectively:

$$\left(\frac{\max(0,\sigma_I)}{S_I}\right)^2 + \left(\frac{\sigma_{II}}{S_{II,E}}\right)^2 = 1 \tag{1}$$

$$\left(\frac{G_I}{G_{IC}}\right)^\alpha + \left(\frac{G_{II}}{G_{IIC,E}}\right)^\alpha = 1 \tag{2}$$

where S_I and $S_{II,E}$ are mode I and mode II strengths, respectively. G_{IC} and $G_{IIC,E}$ are critical strain energy release rates (ERRs). The power $\alpha \in [1,2]$ is an empirical factor derived from mixed-mode tests for interlaminar fracture. $S_{II,E}$ and $G_{IIC,E}$ are 'enhanced'

values due to through-thickness compression [33,34] and are derived by:

$$S_{II,E} = S_{II} - \eta \cdot min(0, \sigma_I) \tag{3}$$

$$G_{IIC,E} = \left(\frac{S_{II,E}}{S_{II}}\right)^2 G_{IIC} \tag{4}$$

where S_{II} and G_{IIC} are the baseline (un-enhanced) mode II strength and critical ERR. η represents the empirical enhancement factor which can be obtained from biaxial tests [35].

One layer of shell elements, each of which had 16 integration points in the thickness direction, i.e. the global *Z*-axis, was employed to describe the shell-element part of the impact model (Fig. 4a). It means that one layer of integration points represents one ply block. A ring-shaped transition part was introduced to transfer DOFs between the solid-element part and the shell-element part, as shown in Fig. 4a. The transition part consisted of three layers of 1 mm long 8-node solid elements along its radius direction, and 8 layers of solid elements in its thickness direction. A penalty-based tied contact was also introduced between the inner surface of the transition zone and the outer surface of the solid-element part. Nodes located at the mid-plane and outer edge of the transition zone were merged with the inner edge of the shell-element part. Each *Z*-direction line of nodes on the outer edge of the transition zone were constrained as a rigid body to have the same DOFs in all three directions. All rigid lines remained straight when subjected to small *Z*-deflection. This implies that each rigid line complies with the classical thin plate theory and allows transfer of all the DOFs between the local (solid-element part) and global domains (shell-element part). The support frame and the impactor were both modelled as rigid bodies, since their deformation is negligible in such tests. The impactor was positioned close to the plate and assigned an initial velocity, which was calculated from the pre-defined impact energy. The impact force was computed from the contact forces generated between the impactor and the plate.

Material properties listed in Table 1 were assigned to each ply-level mesh in the impact model. Cohesive elements for modelling delamination and matrix cracks both had the same material properties, as detailed in Table 2. The transition zone between solid and shell-element parts had homogenised orthotropic material properties that were equivalent to the solid-element part. The measured density of the plate given in Table 1 was used in the impact model. The impact simulation was performed in the FE software LS-DYNA®, as it was shown in [26] and [27] to provide a robust and accurate methodology for predicting delamination and matrix cracking in composites.

3.2. Guided-wave model

The impact model described above employed a global-local mesh to reproduce significant characteristics affecting the impact response of laminates with improved computational efficiency. The guided-wave model in contrast used a uniform mesh of 3D continuum solid elements throughout, in order to avoid spurious wave reflections caused by differences in element size and formulation [36]. As shown in Fig. 4a, each ply block was modelled by a single layer of 0.2 × 0.2 × 0.25 mm^3 (length × width × thickness) eight-node solid elements. The ply material properties listed in Table 1 were also assigned to the guided-wave model. The analytically calculated wavelengths are around 10 mm, 27 mm and 46 mm, respectively for A_0, SH_0 and S_0 modes (Fig. 1). Thus, the selection of element length in the guide-wave model can be considered reasonable, since the shorter wave length of A_0 wave spans more than ten elements [24,37]. In addition, a stiffness-proportional material damping coefficient equalling to 4×10^{-8} was assigned to the guided-wave model. The damping factor was found by iterative calibration to match the experimentally measured attenuation coefficient within 5% error. A comparable value was used in [24,38]. The excitation signal was applied as a *Z*-displacement curve to the surface nodes corresponding to the position of the actuator in experiments. The excitation

signal in the simulation was also a 140 kHz five-cycle sinusoidal tone burst pulse modulated by a Hanning window, while the excitation amplitude was set to the maximum experimental vibration amplitude adjacent to the actuator.

Damage modelling and transfer

Failed interlaminar cohesive elements in the impact model represent predicted delamination patterns, while failed intralaminar cohesive elements represent predicted matrix cracks. The predicted 3D damage information can be transferred to the guided-wave model via the global *X*-*Y*-*Z* coordinate system (Fig. 4a). The volumetric void method used in [21,23,39] was employed to describe delamination, that is to say, a node of the guided-wave model was split into two if it was located in the predicted delamination region, as illustrated in Fig. 5a. In this case, the de-merged nodes were 0.01 mm apart in the *Z*-axis direction. The separation is quite small compared with the wave lengths that its effect on modelling results can be assumed negligible.

As shown in Fig. 5b, if one edge of an element in the guided-wave model was intersected by a matrix crack predicted by the impact model, the element was removed. This allows importing the predicted matrix cracks into the guided-wave model. The element-deletion method used to describe cracks was used in [40] for isotropic materials, but it is here extended for laminates. A zig-zag profile of matrix cracks may be present in ±45° plies, thus a fine mesh was used in this study for better accuracy.

The damage transfer procedure described above was implemented as a MATLAB® code, in order to automate the generation of guided-wave models. It should be noted that this code can also be employed to create guided-wave models by reading damage information from images (i.e. obtained by CT scan), since each pixel/voxel can be interpreted as a ‘finite element’ for the damage transfer procedure.

The FE software Abaqus/Explicit was employed for computing the guided-wave model, as it has a robust combination of solvers and post-processing capabilities. For guided-wave simulations, node-based history outputs were requested instead of element-based field outputs to reduce the amount of data being written to disk. A bespoke Python script was then used to access the output data and re-build the wavefields. This procedure reduced file sizes and improved post-processing speed dramatically. The guided-wave model had 5,997,608 solid elements, while the impact model comprised 7,809 shell elements, 764,696 cohesive elements and 346,966 solid elements. Time step sizes were 2.45×10^{-9} and 6.12×10^{-9}, respectively for the guided-wave model and the impact model. These two models were both run on 32 parallel CPUs in a HPC cluster. With these settings a typical impact model required a wall time of 41 hours, the damage transfer required another 1.5 hours, and the guided-wave model (processing and post-processing) took 7 hours to compute 286 μs of wave propagation.

4. Model calibration and verification

4.1. Impact modelling results

The modelling framework was first validated regarding the predicted impact response. As shown in Fig. 6a, the overall force response in the FE simulation agrees well with experimental measurements. The first significant load drop that corresponds to delamination initiation and the peak load were well captured by the impact model, as are the force oscillations attributed to the damage development. A slight delay was found in the numerical peak force in comparison with experiments, which may be attributed to: (i) the coupling effect between solid elements and shell elements, since a solid-element node has only three translational DOFs while a shell-element node also has three rotational DOFs; and (ii) the slight extra constraint exerted by the four clamps (not modelled) on the dynamic response of the plate. However, the delay in the peak load is expected to

have only minor effects on the damage prediction, because major damage was induced before this peak was reached. The projected delamination area was also well predicted by the FE simulation in general, as shown in Fig. 6b. The impact damage shows an overall symmetry relative to the fibre direction of 0° plies [4,15]. FE results also show that delamination occurred in all the interfaces except the one at the mid-plane, while matrix cracking happened in all the plies except the surface one on the impact side. There existed interconnections of matrix cracks, and interactions between matrix cracking and delamination, as investigated in [28]. A more detailed verification of the impact model can be found in [30,31] and is not repeated here. The considerations above support the validation of the predicted damage data.

The predicted damage was mapped into the guided-wave model using the transfer procedure detailed in Section 3.2. For illustration, the delamination region and matrix cracks respectively associated with the first 90° ply block and corresponding 0°/90° interface on the impact-support side of the plate are presented in Fig. 7, whereby a cross labels the impact centre. Fig. 4a also gives an enlarged view of the guided-wave mesh sectioned along the fibre direction of 0° plies around the impact location, whereby delamination relating nodes are red coded. Considering that the guided-wave model had the same in-plane element size as the interlaminar cohesive mesh in the ROI of the impact model, the predicted delamination could be fully transferred into the guided-wave model without discrepancy. The transfer accuracy for matrix cracks is acceptable since the element in-plane size in the guided-wave model is at least one order smaller than the A_0 wave length and the lengths of all major matrix cracks.

4.2. Ultrasonic modelling results

Global observation

The modelling framework was further validated regarding guided-wave analysis. All

the wavefields presented in this study were acquired from the impactor-side surface of the plate and normalised by the excitation amplitude used in the FE simulation. Figs. 8a-c present the predicted and measured global *Z*-wavefields (formed purely by *Z*-direction vibration) at three points of time after excitation. As demonstrated in Fig. 8a, *Z*-wavefields were dominated by the A_0 mode which propagated along the length of the plate and spread in a circular pattern away from the excitation source. The S_0 mode can also be observed, but the SH_0 mode seems to demonstrate negligible amplitudes from the FE results. The wave amplitude along the fibre directions of ±45° plies is larger than in other directions, because higher bending stiffness is present in these directions [41]. Once the A_0 wave arrived at the damage site it interacted with the damage (Fig. 8b). With further wave propagation the incident wave was reflected by the plate edges (Fig. 8c). The reflected waves interacted with one another as well as the incident wave. This complex behaviour illustrates the difficulty of signal processing for the SHM of laminated structures. The in-plane *X*- and *Y*- wavefields showed very similar global features as the *Z*-wavefield, since these three wavefields formed the overall wavefield through coupling with one another [9]. It is necessary to mention that the in-plane wavefields both had a lower amplitude than the *Z*-wavefield as the plate was excited in the out-of-plane direction.

Fig. 9 quantitatively compares FE predicted and SLV given A_0 phase velocities measured from the excitation centre and along a direction that is within ±60° angle relative to the fibre direction of 0° plies. Wave propagation along a direction beyond ±60° angle is influenced by the short edge of the plate (Fig. 8a), and thus not plotted here. The velocity variance between modelling and experimental measurements was within ±5% for a direction selected in Fig. 9. It can also be observed from Fig. 9 that the wave velocity shows a slightly overall decrease with the maximum value present at around +45° angle,

due to the orientation of the outer plies being at +45° [41]. The small directional dependence of A_0 wave velocity still confirms the quasi-isotropic property of the plate. Additionally, the damping coefficient chosen in the FE model is reasonable since the FE attenuation coefficient given by the FE modelling corresponded to 0.021 m^{-1}, which was 4.5% less than the measured value. The observations given above indicate that the FE simulation is in good agreement with SLV measurements regarding the global wavefield.

Local observation

Local observation of wavefields around the damage area is essential for further verification of the methodology presented in this study. Thus, the wavefields were extracted along four 100 mm long lines, whose middle points are all coincident with the plate centre, as illustrated by blue arrow lines in the guided-wave model plot of Fig. 4a. The monitoring lines follow the fibre directions of 0°, -45°, 45° and 90° plies, and their positive directions are clearly indicated by arrows in Fig. 4a. The local wavefields are then presented in 2-dimensional plots, whereby the horizontal axis represents the time elapsed after excitation, and the vertical axis indicates the distance measured from the negative end of the lines. Figs. 10-12 compare the predicted and measured post-impact *X*-, *Y*- and *Z*-wavefields along the four lines. In-plane wavefields were quantitively underestimated, especially at damage location, however, their overall trends were well predicted. The predicted out-of-plane wavefields show excellent quantitative agreement with experimental measurements, albeit significant reverberations at damage location were observed in experimental plots of Fig. 12. The aforementioned discrepancies between FE and experiments could be attributed to: (i) experimental wavefields were apparently disturbed by noise, which also led to a lower signal to noise ratio in in-plane wavefields than in out-of-plane wavefields; (ii) the impact model was capable of predicting the longest in-plane matrix crack via limiting the crack number to 6 for a ply

block [28], however, shorter cracks may also interact with the ultrasonic wave and affect the wavefield in the damage area; (iii) the wave energy transmission between neighbouring plies through contacts in the delamination region was not simulated in the ultrasonic model, but these contacts may occur and contribute to the local wavefields, since higher wave amplitude was present in the damage region; (iv) each ply block was through-thickness described by one element in the guided-wave model, which allows to accurately predict guided-wave propagation in the undamaged area (see Fig. 9). The prediction accuracy could be improved if multiple elements were used in the damage area, since where most of the plies were disbonded from neighbours, however, the model size would then increase to a non-feasible level regarding the computational capability.

Figs. 10-12 indicate that the A_0 and S_0 modes interacted with discontinuities in the damage area, and this resulted in larger amplitude variation there. The interaction was accompanied by wave transmission, reflection and mode conversion [14,18,42]. A_0 mode was much more sensitive to damage than S_0 mode in all the wavefields, and the former also demonstrated the highest sensitivity when out-of-plane wavefields were considered. From another point of view, the damaged part of the plate can be regarded as a separate pseudo wave source, which continuously dissipated vibration energy. Fig. 13 shows that the FE modelling matches experimental measurements quite well regarding the *Z*-wavefield amplitudes, which were measured over 160 μs after excitation at points located 25 mm and 50 mm away from the damage centre. The Z-wavefield amplitude shows an overall symmetry relative to the fibre direction of 0° plies due to the quasi-symmetric damage profile (Fig. 6b). Experimental data is only plotted at every 45° intervals in Fig. 13 for satisfactory accuracy, considering that the SLV grid resolution was 2 mm. Fig. 13 indicates that the modelling framework is capable of providing valid sensing amplitude data and this is valuable for optimising sensor arrangements in acousto-ultrasonics based

SHM techniques. Overall, all the analysis and discussion given above support the validation of the modelling framework proposed here.

5. Effects of impact damage on guided waves

The proposed modelling strategy was further employed to investigate the overall and individual effects of these two impact damage modes on guided waves, as well as the dependence of guided waves on impact damage extent and multiple impacts. This piece of study was carried out via *Z*-wavefields.

5.1. Effects of overall impact damage

The overall influence of impact damage on guided-wave propagation can be evaluated by the damage-scattered wavefield, which was achieved by subtracting the wavefield acquired with the pristine plate from the one achieved after impact loading. Fig. 14 shows the scattered wavefields along the four monitoring lines (Fig. 4a). The S_0 mode shows a much lower scattered wavefield amplitude than the A_0 mode. The impact-induced damage area is clearly revealed by the A_0 scattered wavefield, since it shows a considerably higher amplitude in the damaged area than in the non-damaged area. The A_0 scattered wavefield is also direction dependent. From an engineering perspective, the damage detection sensitivity should, at least in principle, decrease from the positive 0° direction clockwise and anti-clockwise towards the 90° line. Sensors arranged on the right-hand side of the impact site should give a greater sensitivity than on the left-hand side, with the maximum on the positive side of the 0° line.

5.2. Effects of damage modes

In order to quantify contributions of two damage types (delamination and matrix cracks) to the disturbance of guided wavefields, the modelling procedure was repeated but with the transfer of delamination information only, i.e. suppressing the introduction of matrix cracks. Delamination scattered wavefield can be achieved by subtracting the

pristine-plate wavefield from the delamination-only wavefield. Likewise, the matrix-crack scattered wavefield can be obtained by subtracting the delamination scattered wavefield from the full damage scattered wavefield. These two scattered wavefields along the monitoring lines are quantitatively compared in Figs. 15-16. It can be observed that matrix cracks mainly contribute to the wavefield in the damage region, while delamination reshapes the wavefield in both the damaged and un-damaged regions, especially for the right-hand side of the plate. This can also be confirmed by the similarity observed between the full-damage scattered wavefields in Fig. 14 and the delamination scattered wavefields in Fig. 15. In the damaged region, the delamination scattered wavefield shows a higher amplitude than the matrix-crack scattered wavefield by around 50% on average.

5.3. Effects of damage extent

Guided wavefields following other two energies of impact (10 J and 16 J) were computed using the modelling tool. Fig. 17a compares the predicted damage data for these three impacts in their relative scale. They show similar through-thickness damage profiles, but the overall extents of delamination and matrix cracks both increase with the impact energy. The overall damage area increases by around four times with the impact energy increasing from 10 J to 16 J. Fig. 17b quantitatively compares these three cases regarding full-damage scattered Z-wavefield amplitudes, measured over 160 μs after excitation on a 50 mm radius circle centred at the plate centre. These three cases shows comparable scattering amplitudes, which could be due to their similar damage profiles and the modest increase in overall damage area [24,37]. However, the scattered wave amplitude shows an increase with impact energy in most directions. For a given impact energy, the scattered *Z*-wavefield possesses a larger amplitude on the transmission side than the reflection side [24,37].

5.4. Effects of multiple impacts

The same plate was analysed with two offset 12 J impacts, located 50 mm away from the plate centre along the middle longitudinal line. These two impacts were assumed to have negligible effects on each other regarding the impact response, since the distance between these two sites was much larger than the damage size. Hence, the extents of impact damage were predicted separately using the modelling tool (see Fig. 4a). Firstly, the same excitation signal was introduced into this 'double-damage' plate from the middle of the lower edge. Fig. 18 presents the predicted *Z*-wavefield and corresponding damage-scattered *Z*-wavefields acquired at three time points. Two damage-powered wave sources existed in the double-damage case, and they interacted with the incident wave (Figs. 18a-b) and also with each other (Fig. 18c). This makes NDT in a multiple-damage laminate more complicated than in a single-damage one. It seems very difficult to detect these two damage sites from one sensor installed at the excitation location. The optimum sensing strategy for this case is to install two sensors on these two direct transmission paths. The double-damage model was also run with excitation introduced from the middle of the left short edge. Results show that the incident waves were degraded significantly by the first damage zone (i.e. the left one in Fig. 18), which would cause more difficulties in detecting the second damage, even sensors are installed on the transmission path. This case may require multiple excitation sources. Therefore, establishment of a actuator/sensor network and the relative position of actuators/sensors to potential damage sites are two key factors for the development of ultrasonic guided-wave based NDT and SHM techniques [11,43].

6. Conclusions

This paper has presented a novel numerical modelling framework which integrates high-fidelity predictions of low-velocity impact damage in a composite laminate with the simulation of damage detection via ultrasonic guided waves. The approach incorporates

a meso-scale (ply-level) model of the laminate used to predict low-velocity impact damage, a transient dynamic model that simulates guided-wave propagation in the damaged laminate, and an algorithm that automates the transfer of damage information from the impact model to the guided-wave model. The framework was validated through testing of a carbon FRP plate under low-velocity impact and ultrasonic excitation. The modelling framework showed positive results, in terms of both the global and local wavefields around the damage area. The two most commonly impact-induced damage mechanisms in composite laminates, namely delamination and transverse matrix cracks, were investigated in terms of their influence on the ultrasonic guided wavefield, taking into account extent of damage and the presence of multiple damage sites.

The simulation methodology presented here can be used to estimate the merits and limitations of NDT and SHM techniques for composites based on ultrasonic guided waves, both in terms of impact damage detection as well as damage characterisation. Moreover, this numerical framework can be used in the optimisation of sensor arrangement so that the damage detection sensitivity and reliability can be maximised. This can be done by large numbers of virtual tests using the proposed framework. Future work will focus on applying the methodology to more complex structures and to extend it to higher velocity impact, which will require the incorporation of a fibre failure criterion.

Acknowledgements

This research was conducted as a part of the 'Unlocking the science for an Autonomous Structural Health Monitoring System' project supported by the GW4 Alliance, UK.

References

[1] Richardson MOW, Wisheart MJ. Review of low-velocity impact properties of composite materials. Compos Part A Appl Sci Manuf 1996;27:1123–31.

[2] Ghelli D, Minak G. Low velocity impact and compression after impact tests on thin carbon/epoxy laminates. Compos Part B Eng 2011;42:2067–79.

[3] Koo J-M, Choi J-H, Seok C-S. Evaluation for residual strength and fatigue characteristics after impact in CFRP composites. Compos Struct 2013;105:58–65.

[4] Tan W, Falzon BG, Chiu LNS, Price M. Predicting low velocity impact damage and Compression-After-Impact (CAI) behaviour of composite laminates. Compos Part A Appl Sci Manuf 2015;71:212–26.

[5] De Rosa IM, Santulli C, Sarasini F. Acoustic emission for monitoring the mechanical behaviour of natural fibre composites: A literature review. Compos Part A Appl Sci Manuf 2009;40:1456–69.

[6] He Y, Tian G, Pan M, Chen D. Impact evaluation in carbon fiber reinforced plastic (CFRP) laminates using eddy current pulsed thermography. Compos Struct 2014;109:1–7.

[7] Wang S. Self-sensing of Damage in Carbon Fiber Polymer-Matrix Composite Cylinder by Electrical Resistance Measurement. J Intell Mater Syst Struct 2006;17:57–62.

[8] Tsao CC, Hocheng H. Computerized tomography and C-Scan for measuring delamination in the drilling of composite materials using various drills. Int J Mach Tools Manuf 2005.

[9] Horace L. On Waves in an Elastic Plate. Proc R Soc London Ser A, Contain Pap a Math Phys Character 1917;93:114–28.

[10] Santos MJ, Santos JB, Amaro AM, Neto MA. Low velocity impact damage evaluation in fiber glass composite plates using PZT sensors. Compos Part B Eng 2013;55:269–76.

[11] Ochôa P, Infante V, Silva JM, Groves RM. Detection of multiple low-energy impact damage in composite plates using Lamb wave techniques. Compos Part B Eng 2015;80:291–8.

[12] Toyama N, Takatsubo J. Lamb wave method for quick inspection of impact-induced delamination in composite laminates. Compos Sci Technol 2004;64:1293–300.

[13] Tian Z, Lingyu Yu, Leckey C, Seebo J. Guided wave imaging for detection and evaluation of impact-induced delamination in composites. Smart Mater Struct 2015;24:105019.

[14] Rogge MD, Leckey CA. Characterization of impact damage in composite laminates using guided wavefield imaging and local wavenumber domain analysis. Ultrasonics 2013;53:1217–26.

[15] Leckey CA., Rogge MD, Parker FR. Guided waves in anisotropic and quasi-isotropic aerospace composites: Three-dimensional simulation and experiment. Ultrasonics 2014;54:385–94.

[16] Diamanti K, Hodgkinson JM, Soutis C. Detection of Low-velocity Impact Damage in Composite Plates using Lamb Waves. Struct Heal Monit 2004;3:33–41.

[17] Sohn H, Dutta D, Yang JY, Park HJ, DeSimio M, Olson S, et al. Delamination detection in composites through guided wave field image processing. Compos Sci Technol 2011;71:1250–6.

[18] Ramadas C, Balasubramaniam K, Joshi M, Krishnamurthy C V. Interaction of guided Lamb waves with an asymmetrically located delamination in a laminated composite plate. Smart Mater Struct 2010;19:065009–11.

[19] Sikdar S, Banerjee S. Identification of disbond and high density core region in a honeycomb composite sandwich structure using ultrasonic guided waves. Compos Struct 2016;152:568–78.

[20] Sikdar S, Banerjee S. Guided wave propagation in a honeycomb composite sandwich structure in presence of a high density core. Ultrasonics 2016;71:86–97.

[21] Ng CT, Veidt M, Rose LRF, Wang CH. Analytical and finite element prediction of Lamb wave scattering at delaminations in quasi-isotropic composite laminates. J Sound Vib 2012;331:4870–83.

[22] Ricci F, Monaco E, Maio L, Boffa ND, Mal AK. Guided waves in a stiffened composite laminate with a delamination. Struct Heal Monit 2016;15:351–8.

[23] Hayashi T, Kawashima K. Multiple reflections of Lamb waves at a delamination. Ultrasonics 2002;40:193–7.

[24] Murat BIS, Khalili P, Fromme P. Scattering of guided waves at delaminations in composite plates. J Acoust Soc Am 2016;139:3044–52.

[25] Singh D, Guerjouma R El, Bentahar M. Interaction of fundamental Lamb modes with a point impact damaged zone in composite plates. Proc. Soc. Fr. d'Acoustique, 2012, p. 2423–8.

[26] González E V., Maimí P, Camanho PP, Turon A, Mayugo JA. Simulation of drop-weight impact and compression after impact tests on composite laminates. Compos Struct 2012;94:3364–78.

[27] Feng D, Aymerich F. Finite element modelling of damage induced by low-velocity impact on composite laminates. Compos Struct 2014;108:161–71.

[28] Sun XC, Wisnom MR, Hallett SR. Interaction of inter- and intralaminar damage in scaled quasi-static indentation tests: Part 2 - Numerical simulation. Compos Struct 2016;136:727–42.

[29] ASTM-D7136-07. Standard test method for measuring the damage resistance of a fiber-reinforced polymer matrix composite to a drop-weight impact event. ASTM Int 2007.

[30] Sun XC, Hallett SR. Barely visible impact damage in scaled composite laminates: experiments and numerical simulations. Int J Impact Eng n.d.:Submitted for publication.

[31] Sun XC. Impact modelling of composites. PhD Dissertation, University of Bristol, 2016.

[32] Hallquist JO, Goudreau GL, Benson DJ. Sliding interfaces with contact-impact in large-scale Lagrangian computations. Comput Methods Appl Mech Eng 1985;51:107–37.

[33] Jiang W-G, Hallett SR, Green BG, Wisnom MR. A concise interface constitutive law for analysis of delamination and splitting in composite materials and its application to scaled notched tensile specimens. Int J Numer Methods Eng 2007;69:1982–95.

[34] Li X, Hallett SR, Wisnom MR. Predicting the effect of through-thickness compressive stress on delamination using interface elements. Compos Part A Appl Sci Manuf 2008;39:218–30.

[35] Gan KW, Hallett SR, Wisnom MR. Measurement and modelling of interlaminar shear strength enhancement under moderate through-thickness compression. Compos Part A Appl Sci Manuf 2013;49:18–25.

[36] Bažant ZP, Celep Z. Spurious reflection of elastic waves in nonuniform meshes of constant and linear strain unite elements. Comput Struct 1982;15:451–9.

[37] Ng C-T, Veidt M. Scattering of the fundamental anti-symmetric Lamb wave at delaminations in composite laminates. J Acoust Soc Am 2011;129:1288–96.

[38] Samaratunga D, Jha R. Lamb wave propagation simulation in smart composite structures. 2012 SIMULIA Community Conf., Providence: 2012.

[39] Ramadas C, Balasubramaniam K, Joshi M, Krishnamurthy C V. Interaction of the primary anti-symmetric Lamb mode (Ao) with symmetric delaminations: numerical and experimental studies. Smart Mater Struct 2009;18:085011.

[40] Drozdz MB. Efficient finite element modelling of ultrasound in elastic media. PhD Dissertation, Imperial College of Science Technology and Medicine, 2008.

[41] Maio L, Memmolo V, Ricci F, Boffa ND, Monaco E, Pecora R. Ultrasonic wave propagation in composite laminates by numerical simulation. Compos Struct 2015;121:64–74.

[42] Castaings M, Singh D, Viot P. Sizing of impact damages in composite materials using ultrasonic guided waves. NDT E Int 2012;46:22–31.

[43] Ng CT, Veidt M. A Lamb-wave-based technique for damage detection in composite laminates. Smart Mater Struct 2009;18:074006.

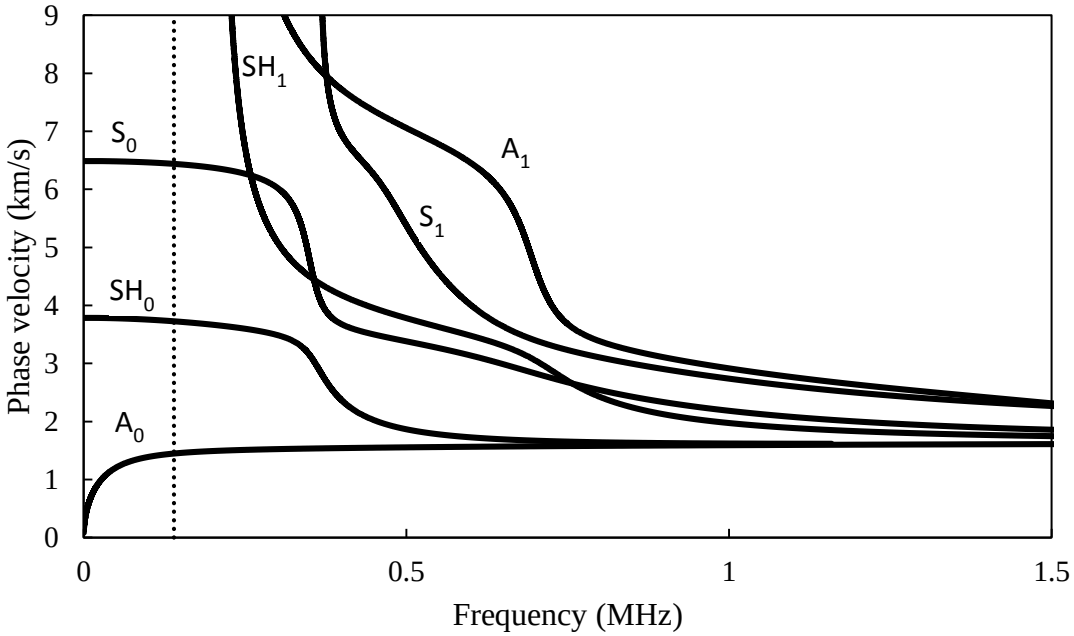

Fig. 1. Analytical dispersion curves of the quasi-isotropic IM7/8552 carbon FRP plate used in this study.

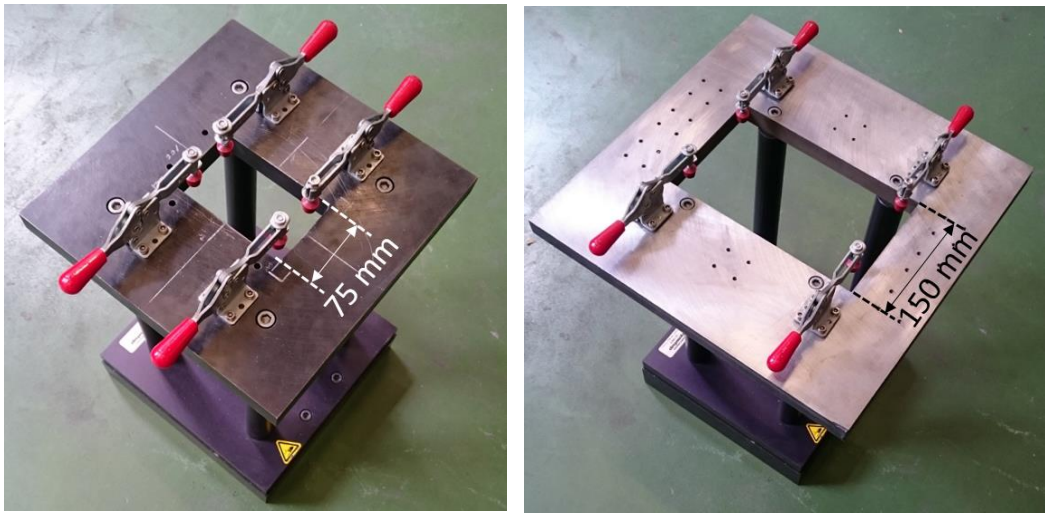

(a) (b)

Fig. 2. (a) The standard support fixture with a 125 mm × 75 mm opening and (b) the larger support fixture with a 250 mm × 150 mm opening used for drop-weight impact tests.

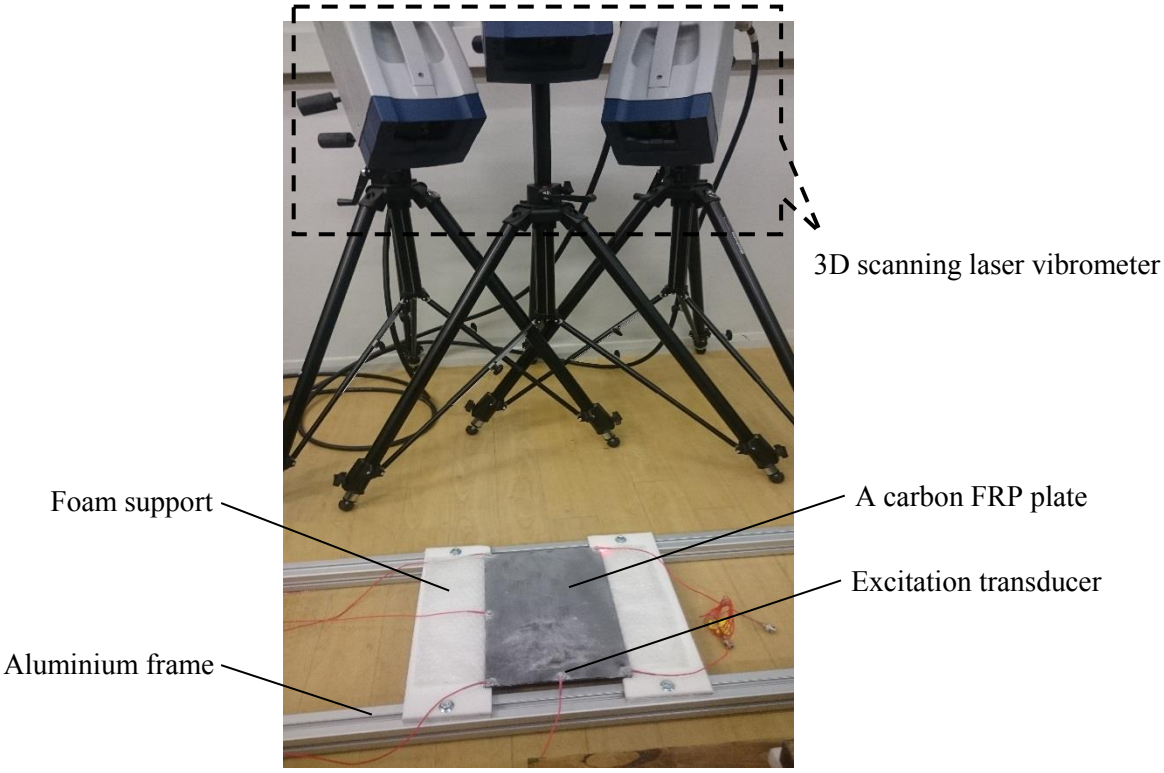

Fig. 3. Experimental set-up for scanning laser vibrometry tests.

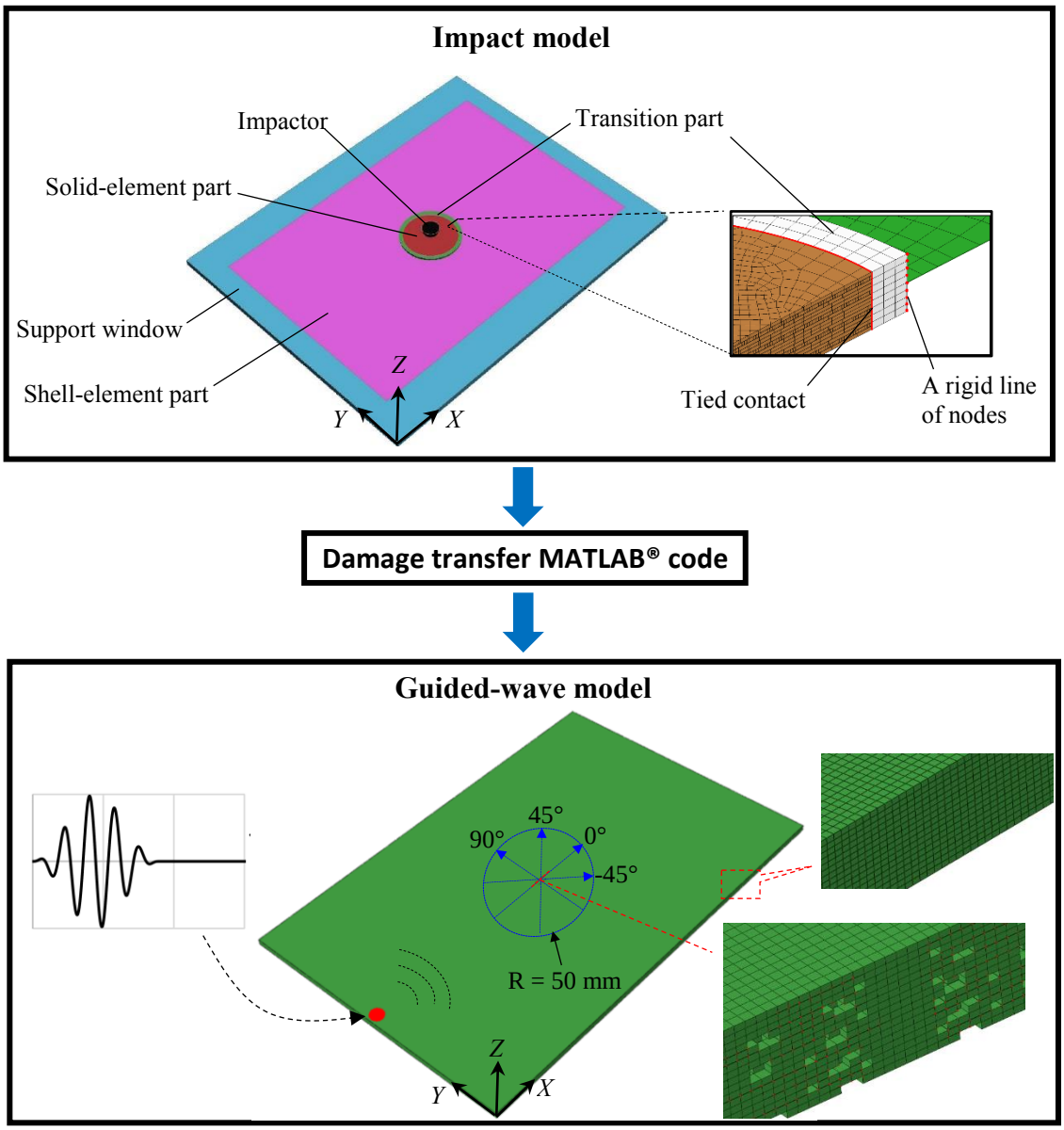

(a)

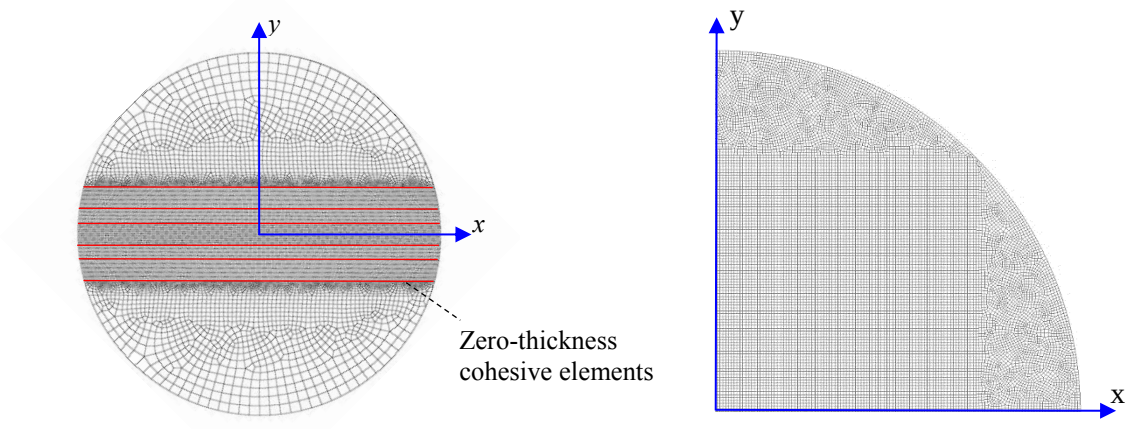

(b) (c)

Fig. 4. (a) An overview of the impact-ultrasonic modelling tool, (b) the ply-level mesh and (c) one quarter of the interlaminar mesh used in the solid-element part of the impact model.

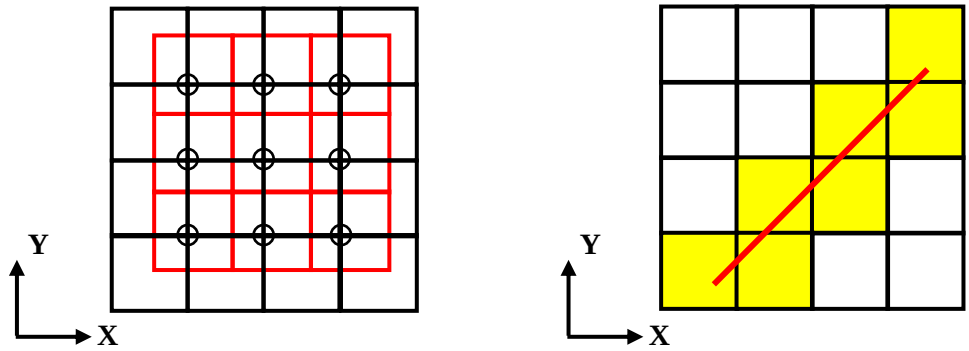

(a) (b)

Fig. 5. Illustration of transfer of impact-model predicted (a) delamination and (b) matrix cracking (both red coded) into the guided-wave mesh (black coded); small circles in (a) indicate released nodes to model delamination; yellow elements in (b) are deleted to model matrix cracks.

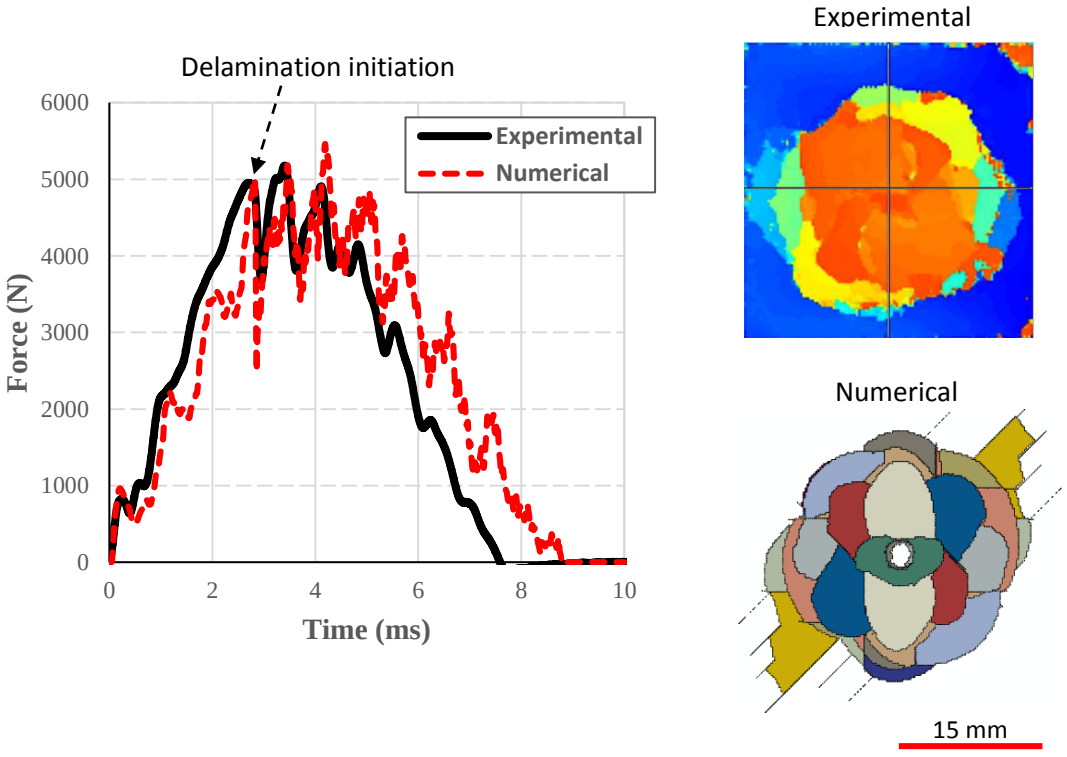

(a) (b)

Fig. 6. Comparison between the impact model and experimental measurements in terms of (a) impact force and (b) volumetric delamination.

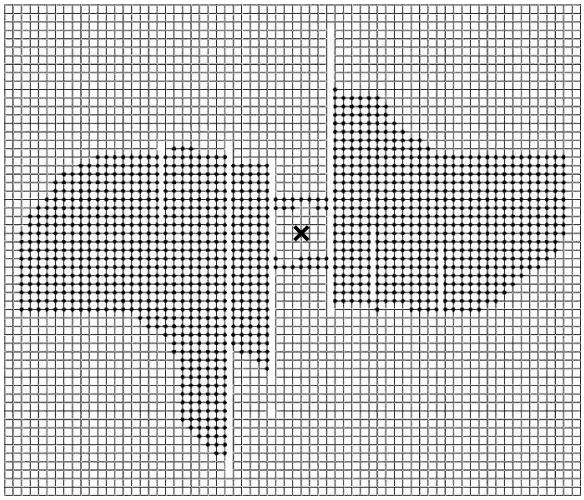

Fig. 7. Numerical descriptions of a 90° ply and associated 0°/90° interface in the guided-wave model; black dots indicate nodes released for delamination; white slots indicate elements deleted for matrix cracks; a cross labels the impact centre.

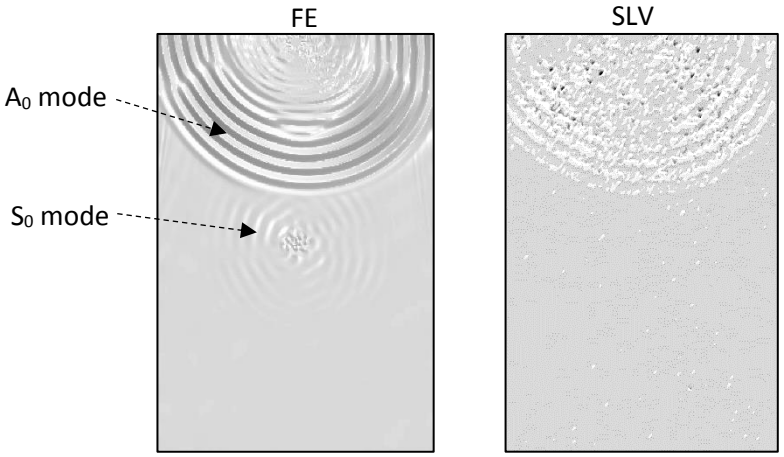

(a)

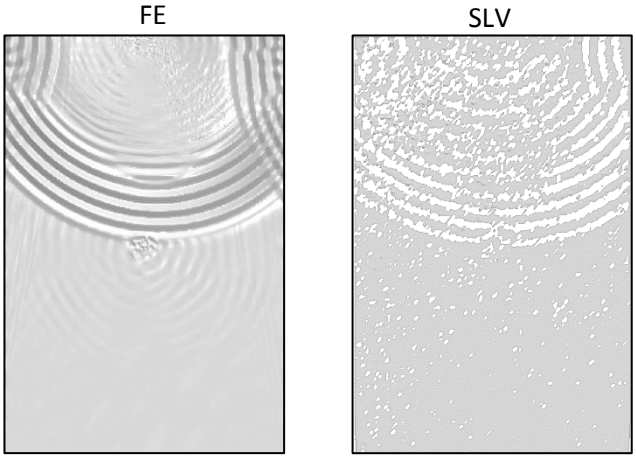

(b)

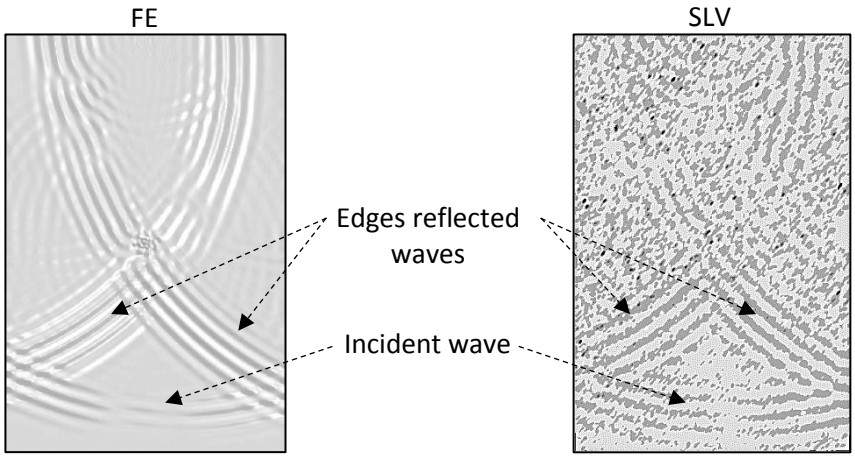

(c)

Fig. 8. Comparison between FE simulated (left) and SLV measured (right) global *Z*-wavefields at (a) 75 μs, (b) 90 μs and (c) 180 μs after excitation.

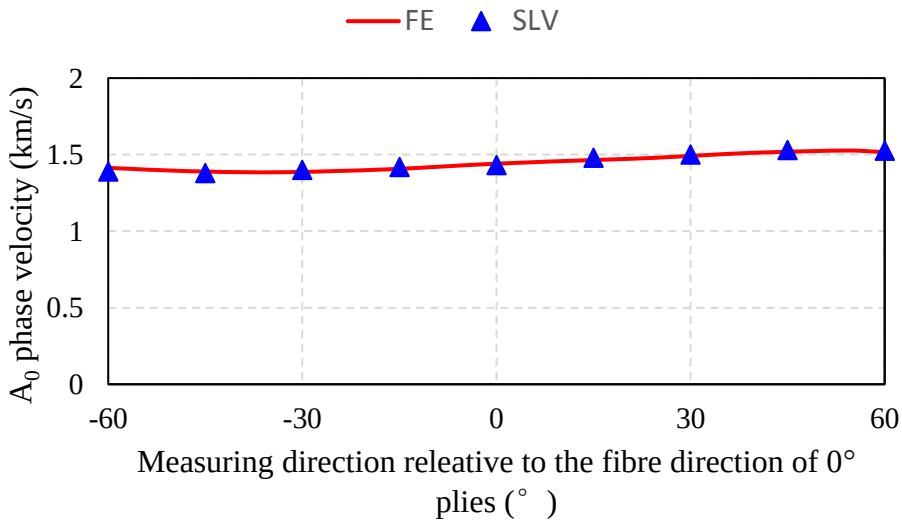

Fig. 9. Comparison of A_0 phase velocities given by FE simulation and SLV measurements under 140 kHz excitation, measured along a direction that is within ±60° angle relative to the fibre direction of 0° plies.

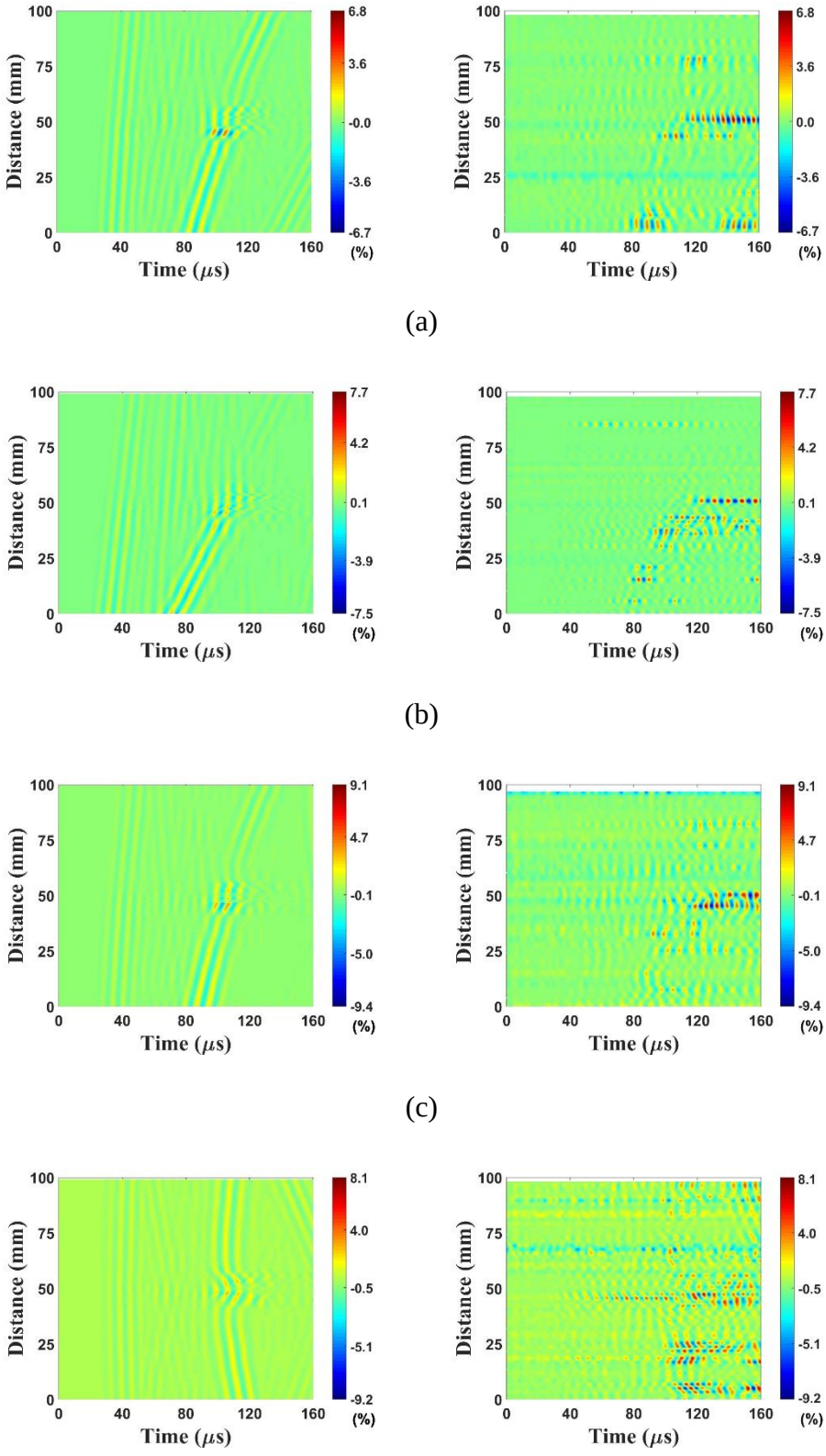

Fig. 10. Local *X*-wavefields acquired after impact by FE simulation (left) and SLV measurements (right) along central (a) -45°, (b) 0°, (c) 45° and (d) 90° lines of the plate.

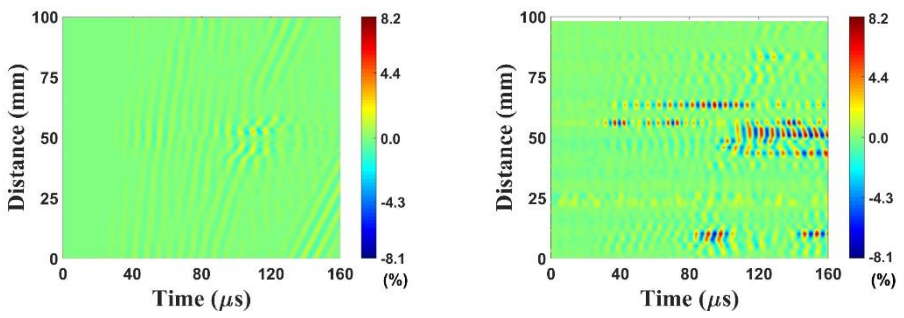

(a)

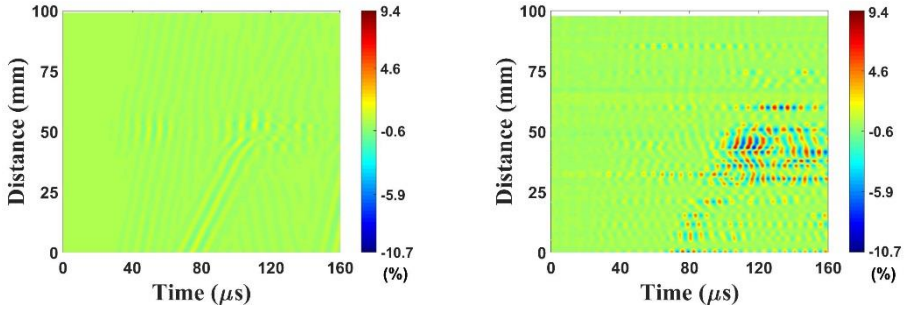

(b)

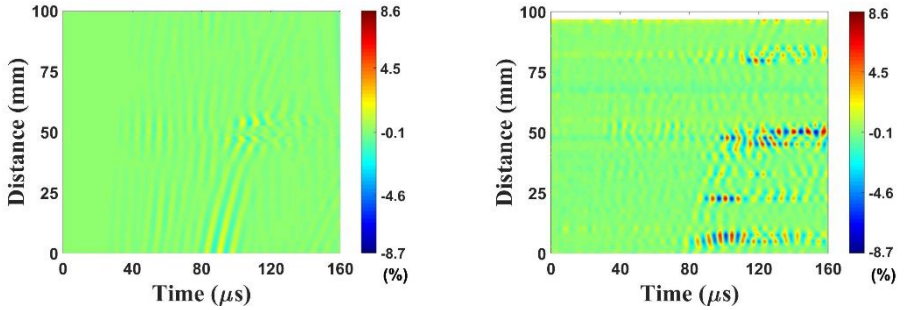

(c)

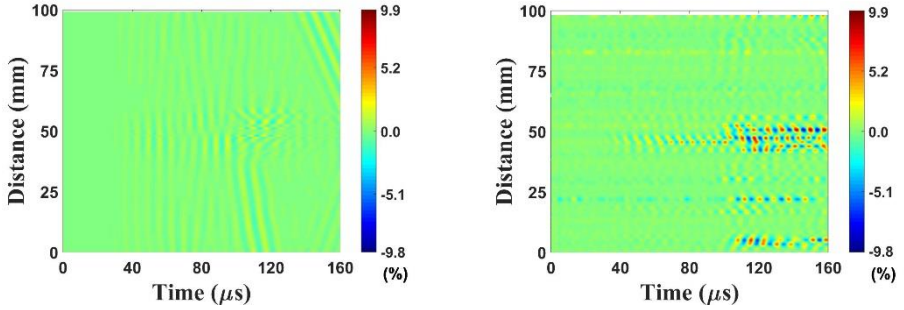

(d)

Fig. 11. Local *Y*-wavefields acquired after impact by FE simulation (left) and SLV measurements (right) along central (a) -45°, (b) 0°, (c) 45° and (d) 90° lines of the plate.

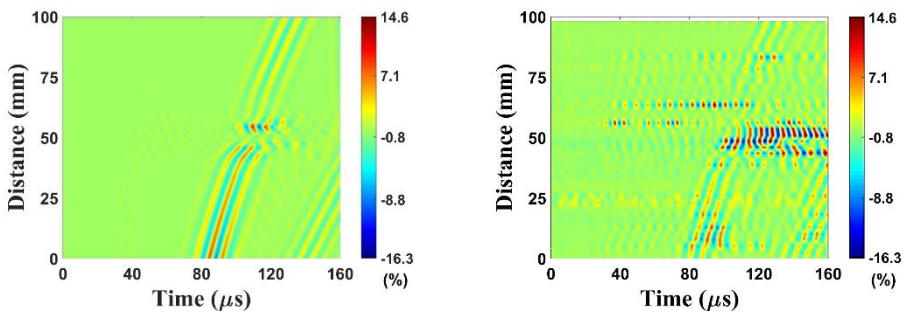

(a)

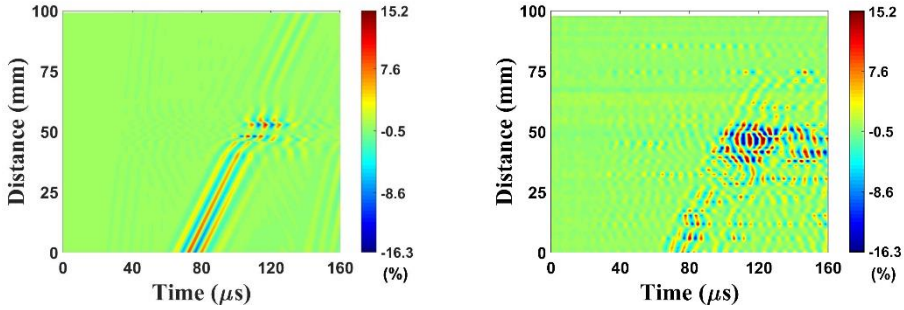

(b)

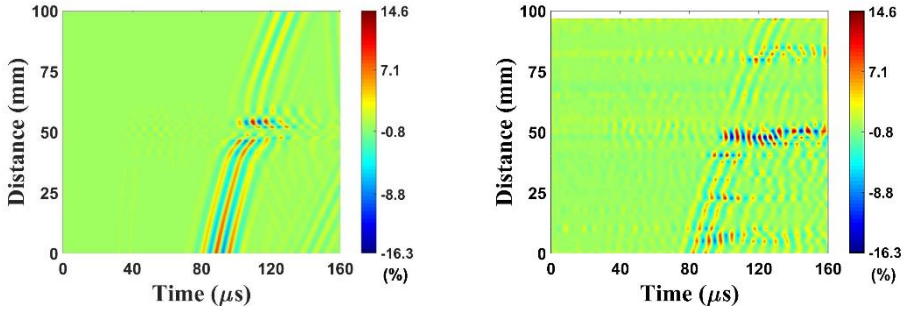

(c)

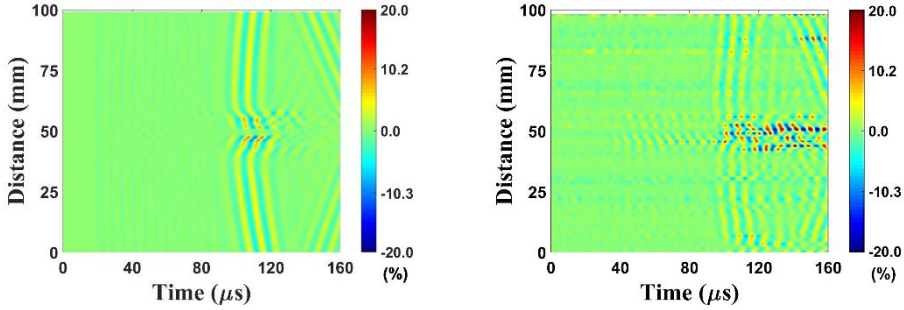

(d)

Fig. 12. Local *Z*-wavefields acquired after impact by FE simulation (left) and SLV measurements (right) along central (a) -45°, (b) 0°, (c) 45° and (d) 90° lines of the plate.

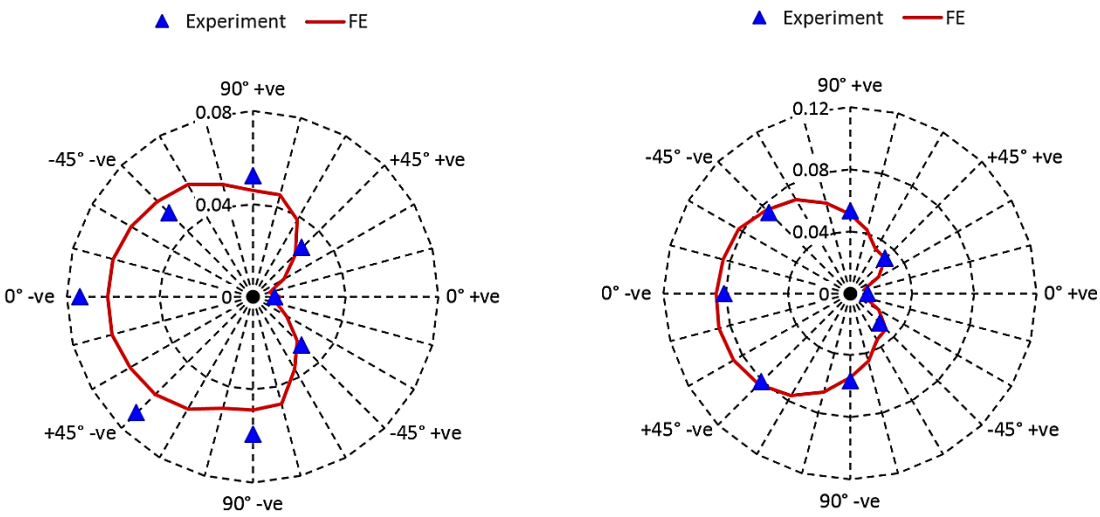

(a) (b)

Fig. 13. *Z*-wavefield amplitudes at the points located (a) 25 mm and (b) 50 mm away from the plate centre, measured over 160 μs after excitation.

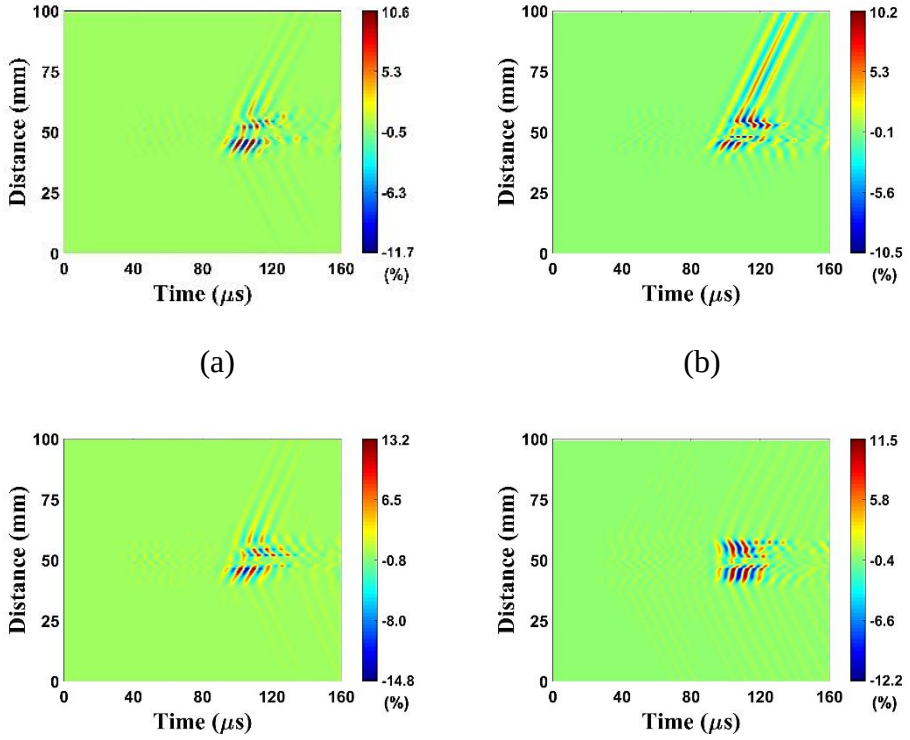

(a) (b)

(c) (d)

Fig. 14. Local damage-scattered *Z*-wavefields predicted along central (a) -45°, (b) 0°, (c) 45° and (d) 90° lines of the plate.

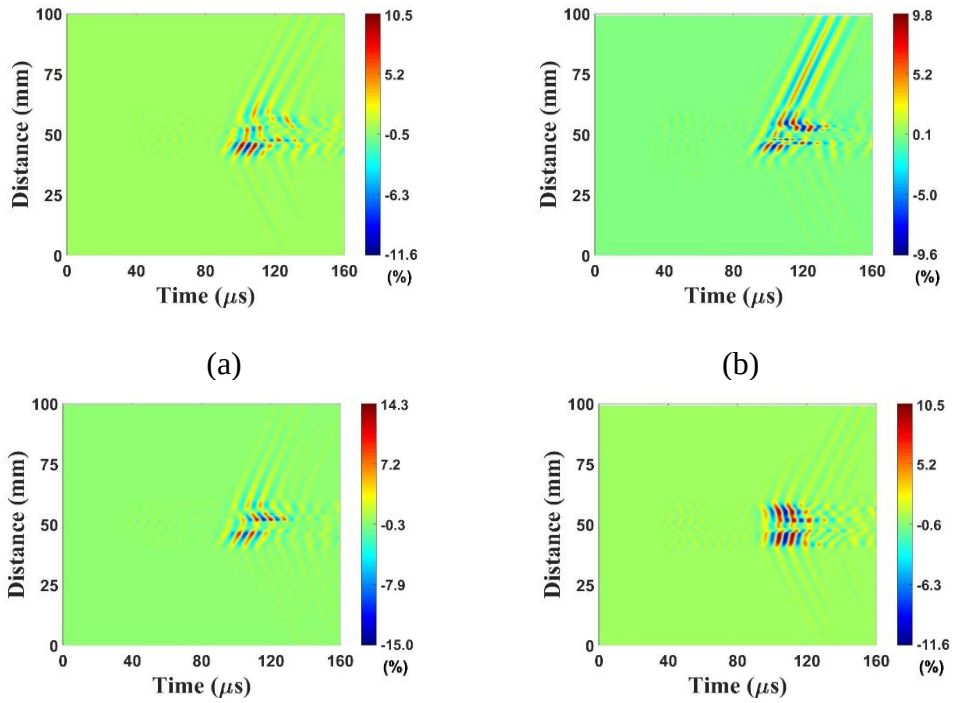

Fig. 15. Local delamination scattered *Z*-wavefields predicted along central (a) -45°, (b) 0°, (c) 45° and (d) 90° lines of the plate.

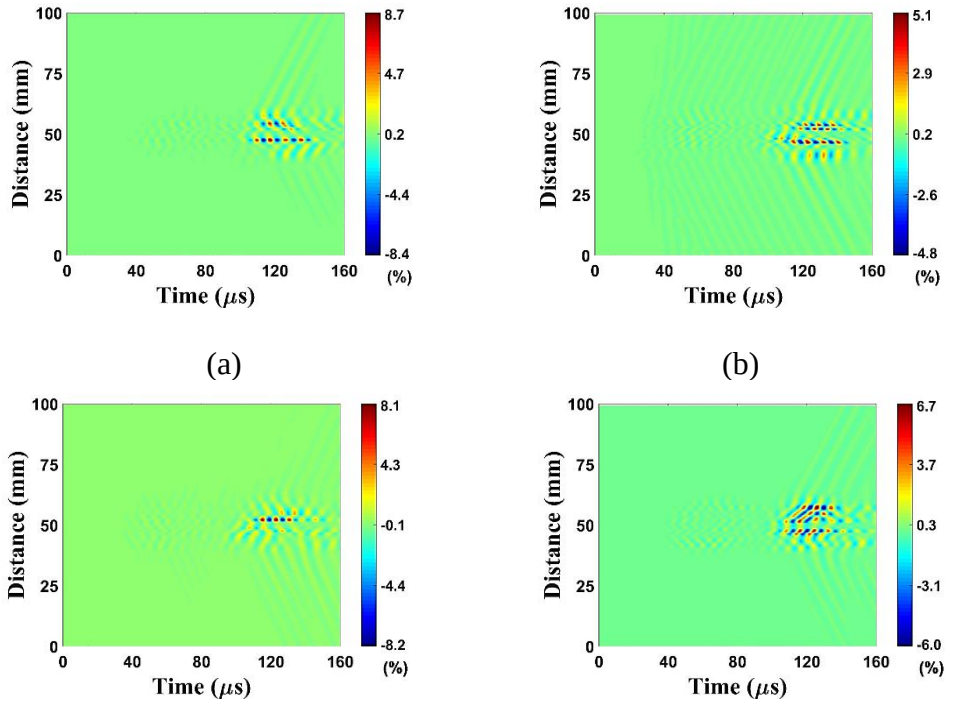

Fig. 16. Local matrix-crack scattered *Z*-wavefields predicted along central (a) -45°, (b) 0°, (c) 45° and (d) 90° lines of the plate.

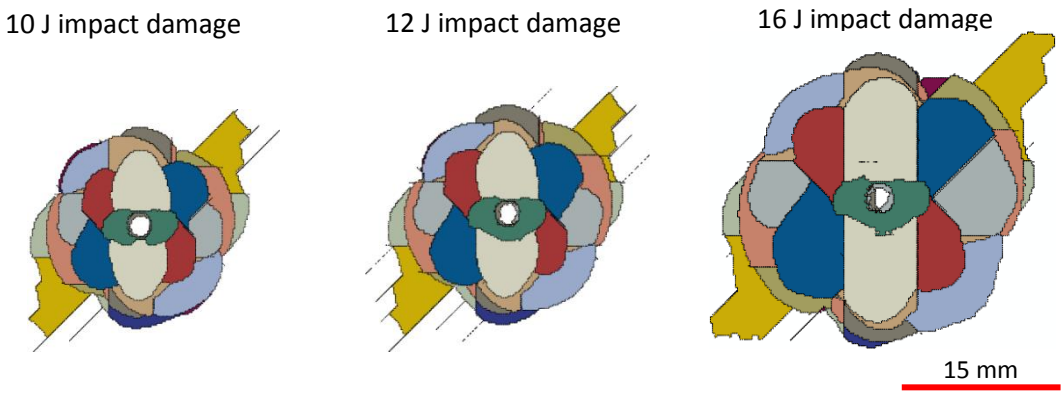

(a)

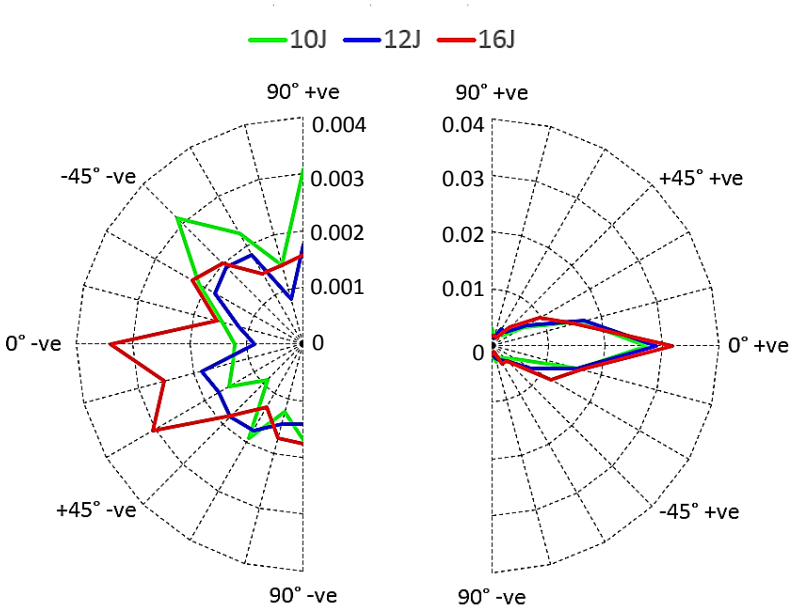

(b)

Fig. 17. (a) Predicted damage profiles and (b) damage-scattered *Z*-wavefield amplitudes for three energies of impacts on a 50 mm radius circle centred at the plate centre.

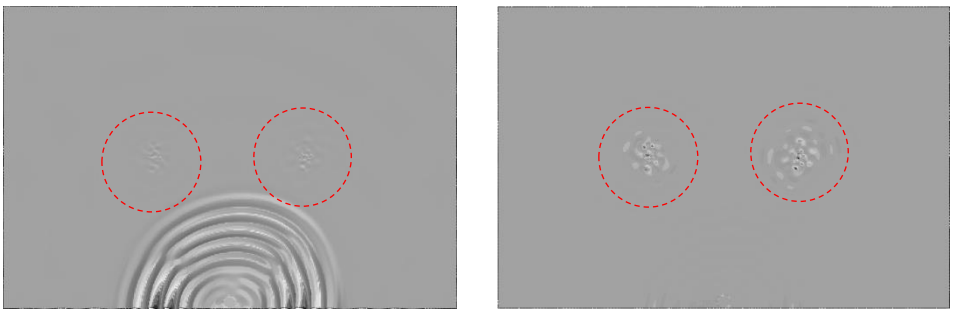

(a)

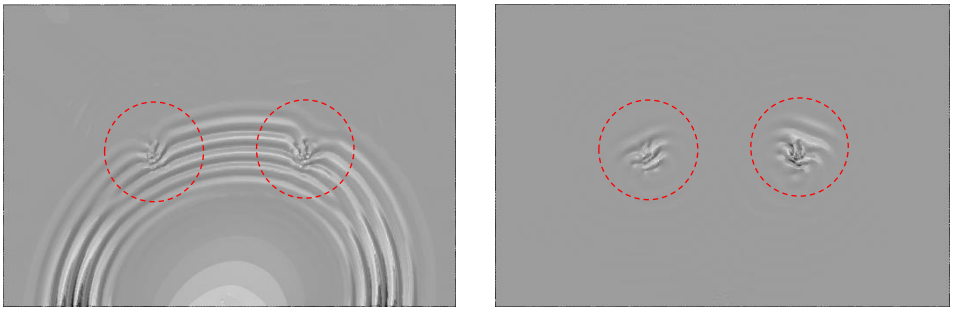

(b)

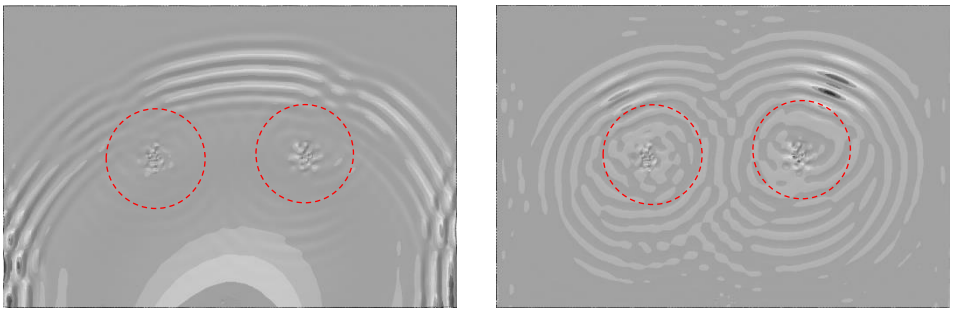

(c)

Fig. 18. Predicted global *Z*-wavefields (left) and corresponding damage-scattered *Z*-wavefields (right) at (a) 48 μs, (b) 83 μs and (c) 114 μs after 140 kHz excitation in a double-damage plate; red circles indicate impact locations.

Table 1. IM7/8552 individual ply properties (1 indicates fibre direction) [28, 30].

E_{11}	$E_{22} = E_{33}$	$G_{12} = G_{13}$	G_{23}	$\nu_{12} = \nu_{13}$	ν_{23}	ρ
161 GPa	11.4 GPa	5.17 GPa	3.98 GPa	0.32	0.436	1626.7 kg/m^3

Table 2. Cohesive properties for modelling delamination and matrix cracks [28, 30].

$K_I = K_{II}$	S_I	S_{II}	G_{IC}	G_{IIC}	α	η
100 kN/mm^3	60 MPa	90 MPa	0.2 N/mm	0.8 N/mm	1	0.3